

This is the peer-reviewed version of the following article:

## X-Ray Imaging with Scintillator-Sensitized Hybrid Organic Photodetectors

Patric Büchele, Moses Richter, Sandro F. Tedde, Gebhard J. Matt, Genesis N. Ankah, Rene Fischer, Markus Biele, Wilhelm Metzger, Samuele Lilliu, Oier Bikondoa, J. Emyr Macdonald, Christoph J. Brabec, Tobias Kraus, Uli Lemmer, and Oliver Schmidt

*Nature Photonics* 9

Subject terms:

Nanoparticles, optical sensors, photonic devices, sensors and biosensors

It has been published in final form at <http://dx.doi.org/10.1038/nphoton.2015.216>.

Patric Büchele<sup>1,2)\*</sup>, Moses Richter<sup>3)</sup>, Sandro F. Tedde<sup>1)</sup>, Gebhard J. Matt<sup>3)</sup>, Genesis N. Ankah<sup>4)</sup>, Rene Fischer<sup>1,3)</sup>, Markus Biele<sup>1)</sup>, Wilhelm Metzger<sup>1)</sup>, Samuele Lilliu<sup>5)</sup>, Oier Bikondoa<sup>6)</sup>, J. Emyr Macdonald<sup>7)</sup>, Christoph J. Brabec<sup>3)</sup>, Tobias Kraus<sup>4)</sup>, Uli Lemmer<sup>2)</sup> and Oliver Schmidt<sup>1)\*</sup>

<sup>1)</sup> Siemens Healthcare GmbH, Technology Center. 91058 Erlangen, Germany

<sup>2)</sup> Light Technology Institute, Karlsruhe Institute of Technology. 76131 Karlsruhe, Germany

<sup>3)</sup> Department of Materials for Electronics and Energy Technology, Friedrich-Alexander University. 91023 Erlangen, Germany

<sup>4)</sup> INM – Leibniz Institute for New Materials, Campus D2 2, 66123 Saarbruecken, Germany

<sup>5)</sup> Masdar Institute of Science and Technology. 54224, Abu Dhabi, United Arab Emirates

<sup>6)</sup> XMaS, The UK-CRG Beamline, ESRF-The European Synchrotron, CS40220. 38043 Grenoble Cedex 9, France

<sup>7)</sup> School of Physics and Astronomy, Cardiff University, Queens Buildings, The Parade, Cardiff CF243AA, UK

\*e-mail: patric.buechele.ext@siemens.com; schmidt.oliver@siemens.com

**Medical X-ray imaging requires cost-effective and high-resolution flat panel detectors for the energy range between 20 and 120 keV. Solution-processed photodetectors provide the opportunity to fabricate large area detectors at low cost. Here, we present a disruptive approach that improves the resolution of such X-ray imaging detectors by incorporating terbium-doped gadolinium oxysulfide (GOS:Tb) scintillator particles into an organic photodetector matrix. The X-ray induced light emission from the scintillating particles is absorbed within hundreds of nanometers, which is negligible compared to the pixel size. Hence, optical cross-talk, currently a limiting factor in the resolution of scintillator-based X-ray detectors, is minimized. The concept is validated with a 256x256 pixel detector with a**

**resolution of 4.75 lp/mm at a MTF = 0.2, significantly better than previous stacked scintillator-based flat-panel detectors. We achieved a resolution that proves the feasibility of solution-based detectors in medical applications. Time-resolved electrical characterization, showed an enhanced charge carrier mobility with increased scintillator filling fraction, which can be explained by morphological changes at the interface GOS:Tb/organic bulk hetero-junction.**

Today's most common flat-panel X-ray detectors for medical imaging consist of a scintillator that converts X-ray photons into light and a photodetector array made out of amorphous silicon to detect<sup>1,2</sup>. The light emitted from the scintillator then propagates isotropically from the point of generation. This causes optical crosstalk between pixels, resulting in a low resolution. In addition to optical cross-talk, the detectors resolution is also limited by pixel size and electrical cross-talk e.g. due to trapped charges<sup>3</sup>. The resolution can be described with the modulation transfer function (MTF), which describes the detector's ability to transfer the input signal modulation of a given spatial frequency in relation to its output. An MTF value of 1 indicates a perfect detection of a given spatial frequency. In order to compare different detectors it is practicable to determine the value of the spatial frequency  $f$  (measured in linepairs (lp) per mm) at which the MTF drops to 0.2. Advanced scintillators, such as thallium doped cesium iodide (CsI:Tl), have a needle-type structure that behaves as a waveguide and decreases the optical crosstalk<sup>4</sup>, resulting in  $f = 2-3$  lp/mm at MTF = 0.2, depending on the thickness of the CsI:Tl<sup>1</sup>. However, CsI:Tl deposition is an expensive process and the material loses its crystal structure, when exposed to humidity<sup>5</sup>.

Direct-conversion detectors consist of a semiconductor material such as amorphous selenium (a-Se) that provides a high intrinsic X-ray absorption coefficient<sup>6</sup>. Because X-rays generate charges directly inside of the semiconductor, these detectors have almost no optical crosstalk. While their resolution can be very high, it is limited by pixel size, electrical cross-talk and the operating electrical field. Current a-Se detectors have achieved  $f = 4.75$  lp/mm at MTF = 0.2<sup>7</sup>. The field dependence of the ionization energy and the weak X-ray absorption necessitate thick layers and unacceptably high operating voltages to achieve the electrical field required for an efficient charge extraction ( $\sim 30$  V/ $\mu\text{m}$ )<sup>8</sup>.

Recently, several concepts have been proposed to leverage the advantages of organic semiconductors in medical flat panel X-ray detectors requiring a size of up to  $43 \times 43 \text{ cm}^2$ <sup>9</sup>. Organic

photodiodes (OPDs) are attractive and cost-effective for this application as they can be processed from the solution phase over large, even flexible, substrates<sup>10,11</sup>. OPD technology is based on an interpenetrating donor-acceptor network of an electron conductor, e.g. phenyl-C61-butyric acid methyl ester (PCBM), and a hole conductor, e.g. poly(3-hexylthiophene-2,5-diyl) (P3HT), which is known as the bulk-heterojunction (BHJ)<sup>12</sup>. When a photon is absorbed by the BHJ, a Frenkel exciton is generated and can travel to the donor-acceptor interface, where it splits into an electron and a hole. The free charges can diffuse through the donor and acceptor percolation paths and reach their respective electrodes, thus enabling photodetection<sup>13,14,15</sup>.

Appropriate nanoparticles can sensitize the absorption spectrum of pure P3HT:PCBM blends from the near infrared to the X-ray region. Recently, OPDs have been enhanced with lead sulfide quantum dots for near-infrared detection<sup>16</sup>. Likewise, X-ray detection was demonstrated by adding small amounts of metal nanoparticles into a hole-conducting polymer<sup>17</sup>.

## Results and discussion

In this paper, we demonstrate that scintillating terbium-doped gadolinium oxysulfide (GOS:Tb) X-ray absorbers in the BHJ create a quasi-direct X-ray detector. The re-emitted photons from the scintillator particles are absorbed by the BHJ very close to the scintillator, minimizing optical crosstalk and enabling a high MTF. Low-cost micrometer-sized scintillator particles are used to achieve an optimum balance between large X-ray absorption and efficient charge extraction. The attenuation of GOS:Tb is above that of CsI:Tl for X-rays <33 kV and >50 kV<sup>1</sup>. The concept allows for adapting the scintillator/polymer material composition to the hardness of the radiation and is not limited to scintillators with anisotropic structures such as CsI:Tl.

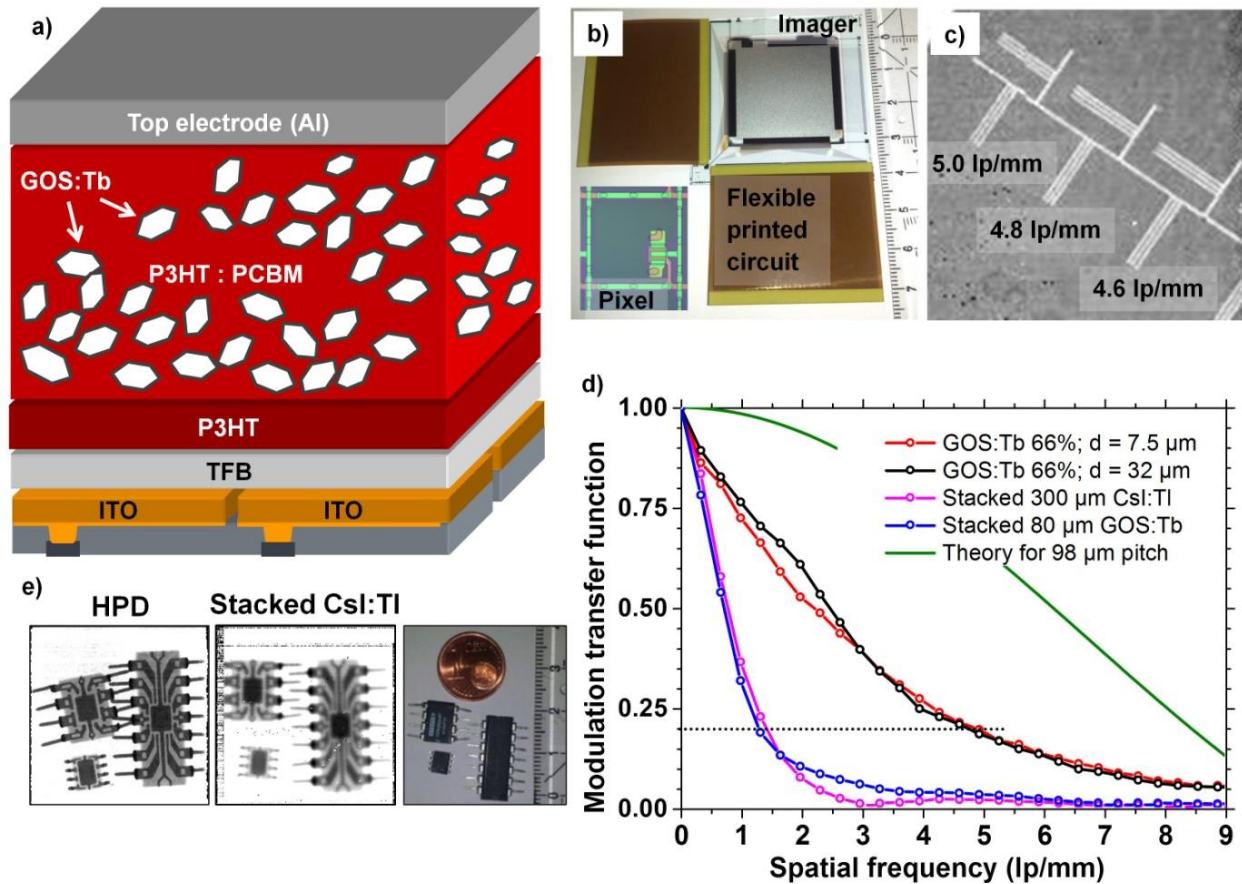


**Figure 1 | Hybrid organic X-ray image sensor.** a) Schematic of the image sensor with an a-Si:H backplane and a hybrid frontplane. b) Photograph of a fully processed imager and micrograph of an individual pixel with one TFT (98µm pitch). c) 70kV X-ray image (magnified region of interest) of a resolution test target. d) MTF of HPD-imagers with different layer thickness and two conventional indirect X-ray converters. The theoretical limit is determined by the pixel size. e) 70 kV X-ray images of integrated circuit devices realized (photograph on the right) with an HPD image sensor (left) and a conventional stacked device (center).

We fabricated several X-ray image sensors with the structure depicted in Fig. 1a. The devices were based on an a-Si:H TFT array backplane with indium tin oxide (ITO) contact pads. Two interlayers of poly[(9,9-dioctylfluorenyl-2,7-diyl)-co-(4,4'-(N-(diphenylamine)]-butylphenyl)) (TFB) and P3HT were subsequently deposited on the backplane to reduce the dark current. Both interlayers form hole extracting/electron blocking contacts; in addition the low intrinsic conductivity, efficiently reduces electrical cross-talk (i.e. between photodiodes). A suspension containing P3HT, PCBM and GOS:Tb was deposited on the interlayer by spray-coating. The device stack was finalized by an electron selective aluminum (Al) top contact, deposited by thermal evaporation. The devices were encapsulated with epoxy glue and glass to avoid oxidation of the BHJ and Al

electrode. Degeneration of the organic matrix upon X-ray irradiation was observed, but the effect was small, reversible by thermal treatment, and not a significant problem for medical X-ray imaging sensors<sup>18</sup>. A completed X-ray image sensor is shown in Fig. 1b.

The backplane matrix consists of  $256 \times 256$  pixels with a pixel pitch of  $98 \mu\text{m}$ , a geometric fill factor of  $\sim 70\%$  and the pixel structure shown in the inset of Fig. 1b. A portion of the X-ray image of a resolution test target provided by using such a detector is shown in Fig. 1c. The image was recorded with an X-ray beam generated with 70 kV tungsten bremsstrahlung spectrum and filtered with 2.5 mm aluminum (dose rate  $10 \text{ mGy}_{\text{air}}/\text{s}$ , integration time  $\sim 22 \text{ ms}$ , resulting in a dose of  $220 \mu\text{Gy}_{\text{air}}$ ). The resolution test target consisted of linepairs in a lead layer with a feature density between 4 and 5 lp/mm, all of which were resolved by the detector. The noise of our detectors was limited by a non-optimal read-out circuitry with a noise level of 8.000 electrons and the relatively high dark current of our detector. Further X-ray images and shelf-life measurements are reported in the Supplementary Information (see Fig. S1-S2).

The slanted edge method measures the MTF to provide a quantitative resolution value<sup>19</sup>. Fig. 1d demonstrates that, for our hybrid photodetectors (HPDs), the resolution does not change with increasing thickness of the X-ray absorbing layer between  $7.5 \mu\text{m}$  to  $32 \mu\text{m}$ . Preliminary results (data not shown) with a  $170 \mu\text{m}$  thick layer showed similar resolution. The spatial frequency, at which the MTF drops to 0.2 was 4.75 lp/mm, which is comparable with a state of the art a-Se detector<sup>7</sup>. The resolution of our demonstrator lies below the theoretical limit, likely due to pixel-to-pixel and trap-assisted electrical cross-talk that are known from direct converters. Our hybrid detector clearly outperforms indirect converters with stacked scintillator ( $80 \mu\text{m}$  GOS:Tb and  $300 \mu\text{m}$  CsI:Tl) mounted on top of an OPD, as is clear in the side-by-side comparison of X-ray images of integrated circuits in Fig. 1e.

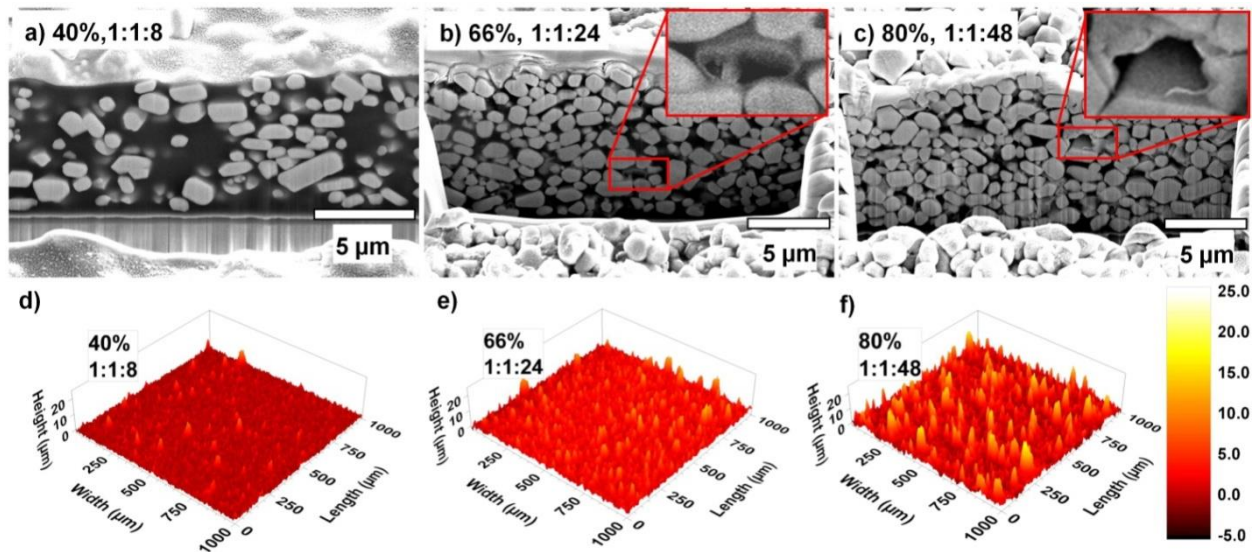


**Figure 2 | Influence of scintillator fraction on layer morphology.** a-c) SEM cross-sections (FIB cuts with 52°-tilt angle perspective view), red boxes and insets highlight voids inside of the devices and d-f) 3D surface profilometry of samples with 40 vol.%, 66 vol.% and 80 vol.% GOS:Tb. Scanning resolution is 1 μm in both axis.

In the following, we use test diode structures to study the fundamental physical properties and limitations of HPDs. The scanning electron microscopy (SEM) images in Fig. 2a-c show cross-sections of HPDs prepared with a focused ion beam (FIB) sections with three different volume ratios of the GOS:Tb: 40 vol.% (the weight ratio of P3HT:PCBM:GOS:Tb was 1:1:8), 66 vol.% (1:1:24) and 80 vol.% (1:1:48). Isolated GOS:Tb particles (bright) are surrounded by a homogeneous P3HT:PCBM BHJ (dark). The GOS:Tb particles were fully embedded in the organic matrix for samples with 40 vol.%, while voids (marked with red boxes) occurred increasingly at higher fractions of GOS:Tb due to the limited amount of organic material. X-ray absorption increased with GOS:Tb content up to a 66 vol.%. At higher GOS:Tb fractions, the packing density of the solid particles limited their final volume fraction, caused the formation of voids (see Fig. S3), and X-ray absorption saturated.

From an optical perspective, the optimum volume ratio between particles and BHJ depends on the particles' emission and the BHJ's absorption properties. The dominating green emission of X-ray excited GOS:Tb has a large overlap with the absorption spectra of P3HT:PCBM (see Fig. S4), which results in a small penetration depth (130 nm). A core-shell model that assumes an average size for the GOS:Tb particles (1.8 μm diameter) predicts an ideal volume ratio between X-ray

converting GOS:Tb cores and photon-absorbing BHJ shells of 67 vol.%. Particle contents below this “golden filling factor” limit X-ray absorption and the generation of charge carriers, while particle concentrations above perturb the extraction of photogenerated charge carriers. The 3D profiles also show that the detector surfaces become rougher with increasing GOS:Tb fractions (cf. Fig. 2d-f). Excess GOS:Tb at the top surface aggregates during the spray coating process and inhibits the formation of a good metal contact. The resulting defects at this interface play an important role in the following discussion.

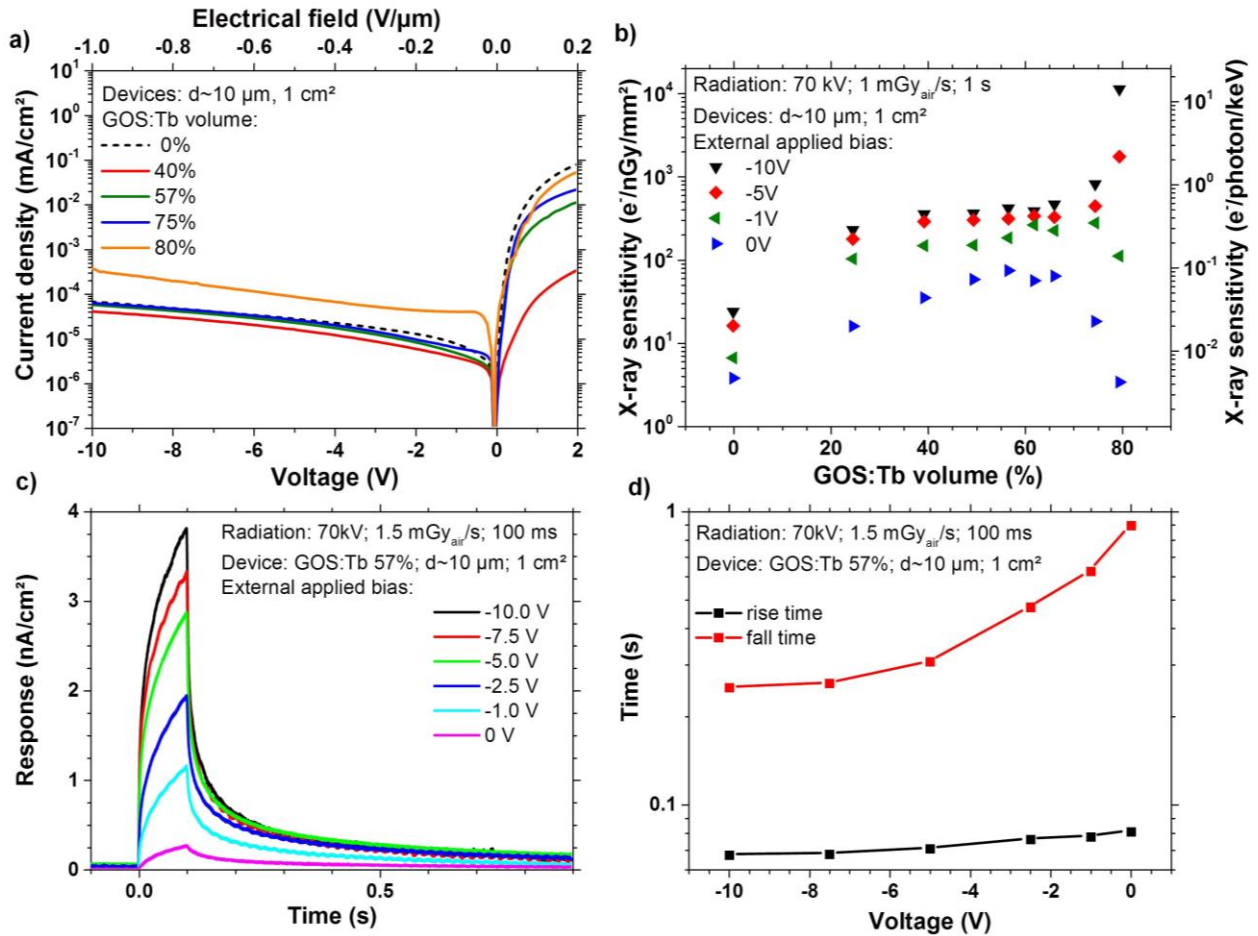


**Figure 3 | Optoelectrical properties of HPDs.** a) Dark IV-characteristics with different GOS:Tb volume fractions and an active area of 1 cm<sup>2</sup>. b) X-ray sensitivity (left axis in e<sup>-</sup>/nGy/mm<sup>2</sup>, right axis in e<sup>-</sup>/photon/keV) irradiated with a spectrum of 70kV bremsstrahlung and dose rate of 1 mGy<sub>air</sub>/s at different external bias. c) Pulse response of the 57 vol.%-HPD biased from 0 V to -10 V (0 V/μm to -1 V/μm); dose rate: 1.5 mGy<sub>air</sub>/s, 100 ms pulse duration. d) Corresponding rise and fall time dependent on the applied bias.

We studied the effect of the filling factor on the electrical properties and the X-ray response. The amount of GOS:Tb in the dispersion was gradually increased from a weight ratio between P3HT:PCBM:GOS:Tb of 1:1:0 (0 vol.%) up to 1:1:48 (80 vol.%). Test devices with the same layer stack as described above and a diode area of 1 cm<sup>2</sup> were processed and characterized electrically in the dark and under X-ray irradiation. The dark current density in reverse bias of HPDs was an important measure for the minimal detectable signal and should be as low as possible. Fig. 3a shows virtually identical dark current densities under reverse bias for all devices except for the 80 vol.% device, which was likely to be dominated by defects at the interface to the top contact (see Fig. 2c and 2f). The injected current-density at forward bias (Al contact was negative in respect to the ITO) increases with a higher GOS:Tb filling fractions. This is unexpected - the addition of insulators to the device should not improve charge carrier transport. The pure 0 vol.% P3HT:PCBM device showed the highest rectification. As outlined later in detail, the morphology and consequently the nature of the charge-transport of the BHJ, changes dramatically by the addition of the GOS:Tb particles.

An important sensitivity measure of an HPD is the response to X-ray radiation. Fig 3b shows the X-ray sensitivity  $S$  of our samples:

$$S = \frac{Q}{e \cdot D \cdot A} = \frac{\int I_{X\text{-ray}}(t) - I_{\text{dark}} dt}{e \cdot D \cdot A} \quad (1)$$

where  $I_{X\text{-ray}}$  and  $I_{\text{dark}}$  represent the current under X-ray irradiation and in the dark, respectively,  $e$  represents the elementary charge,  $D$  the X-ray entrance-dose-in-air, which is commonly used in medical applications to calculate the patient or organ dose<sup>20</sup> (defined in detail in the Supplementary Information), and  $A$ , the active area of the HPD. The equation expresses the number of extracted charge carriers  $Q/e$  generated by X-ray radiation per entrance-dose-in-air  $D$  and per irradiated area of the hybrid layer  $A$ . At low filling ratios,  $S$  increased with the fraction of GOS:Tb due to increasing X-ray absorption. At a bias of 0 V,  $S$  had a maximum at a GOS:Tb fraction of around 60 vol.%, close to the golden filling factor discussed above. It decreased at higher GOS:Tb loading due, to degrading charge transport in the remaining BHJ.

An external bias of -10 V increased  $S$  in detectors with little GOS:Tb by almost one order of magnitude because of the bias improved charge carrier extraction. In detectors with GOS:Tb contents above the golden filling factor,  $S$  increased dramatically when an external field was

applied. This may be explained by a photoconductive gain mechanism, as reported before<sup>21</sup>. The electric field density was more concentrated in the organic phase and the increasing roughness with higher GOS:Tb fraction additionally increases field-emission at the aluminum contact<sup>22,23</sup>. Morphological changes (vide infra) at high filling ratios likely cause an unbalanced transport behavior. We observed slow reaction times (see Fig. S7) and a photoconductor-type response (see Fig. S8) at high GOS:Tb contents.

An X-ray sensitivity of  $S = 360 \text{ e}^-/\text{nGy}/\text{mm}^2$  for the 50 vol.% HPD device at  $-10 \text{ V}/\mu\text{m}$  corresponds to an electron-hole-pair generation energy of 68 eV (see Supplementary Information for details), which is slightly larger than an a-Se direct converter at an electrical field of  $10 \text{ V}/\mu\text{m}$ <sup>6</sup>.

The pulse response time is an important factor when imaging dynamic objects with short X-ray pulses. The transient current response of the 57 vol.% device upon X-ray irradiation is plotted in Fig. 3c. X-ray pulses with a dose rate of  $1.5 \text{ mGy}_{\text{air}}/\text{s}$  and a pulse duration of 100 ms were applied and the bias was varied between 0 V and -10 V ( $0 \text{ V}/\mu\text{m}$  and  $-1 \text{ V}/\mu\text{m}$ ). The dark current was subtracted for better comparison. Fig. 3d shows that the rise time (from 10 % to 90 % of the maximum signal) and the fall time (from 90 % to 10 %) decreased for higher bias. There was no saturation of the current response within the pulse length of 100 ms for any bias: Arguably trap states at the metal/semiconductor interface are responsible for the slow response<sup>24,25</sup>.

The remaining technological challenges are the relatively high dark current density and the slow response time. Both depend crucially on oxygen doping induced during spray-coating in ambient conditions and interface traps between the electrodes and semiconductor<sup>26</sup>. Both will be addressed by workfunction and interlayer tuning as well as by oxygen-free deposition methods<sup>27</sup>.

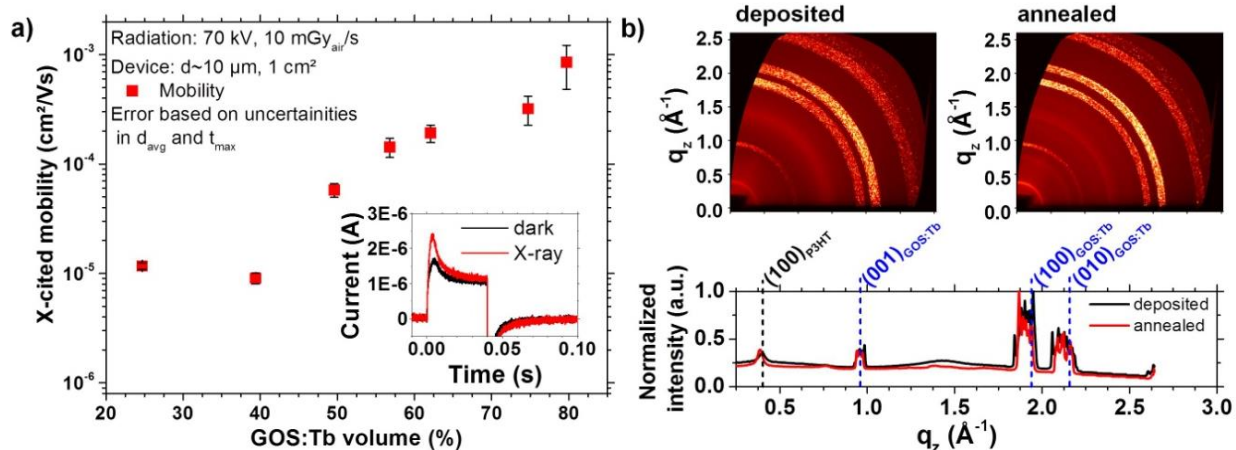


**Figure 4 | Mobility and morphology characteristics.** a) X-CELIV properties with different GOS:Tb volume fraction. The inset represents a typical X-CELIV peak. b) GI-WAXS Debye-Scherrer-rings and out-of-plane line profiles  $a_i = 0.24^\circ$ ,  $\chi = 15^\circ$  of the 57 % (1:1:16) HPD as deposited and annealed. Intensity has been normalized, while the x-axis represents the absolute value of the scattering vector  $q_z$ .

A new method was required in order to analyze the charge transport mechanism of the thick HPDs. For this purpose, we developed “X-ray excited Charge carrier Extraction by Linearly Increasing Voltage” (X-CELIV) to probe the mobility of X-ray-generated charges by measuring the transient current during a voltage ramp. In X-CELIV, charge carriers are excited throughout the bulk layer which opens the possibility of studying an HPD, similar to photo-CELIV<sup>28</sup>. In X-CELIV the mobility of the X-ray generated free charge-carriers, are measured by analyzing the temporal charge extraction upon depletion of the sample. Charge carrier depletion is achieved by applying a voltage ramp (e.g. from 0V to 20V). The elegance of the CELIV method lies in the fact, that the sample is analyzed under the actual working conditions and no further sample preparations/modifications are necessary. The inset in Fig 4a. shows a representative X-CELIV signal in dark (black graph) and after an X-ray pulse (red graph). The X-CELIV signal can be divided into two main features, a relatively rapidly increasing signal followed by a slower decay, and second signal of a constant positive offset (boxcar function). This offset describes the displacement current of the sample capacitance, whereas the extracted charge-carriers from of the sample causes the first mentioned “extraction peak”. After X-ray exposure, an enhanced extraction peak due to the increased free charge carrier concentration is observed, and the maximum is shifted to a shorter time scales.

The effective drift mobility of the excited free charges in the P3HT:PCBM is calculated from the time delay of the peak maximum relative to the onset of the rectangular signal<sup>29,30,31</sup>. Fig. 4a shows the charge carrier mobility as function of the GOS:Tb volume fraction. The mobility increased by two orders of magnitude when varying GOS:Tb fractions between 25 vol.% and 80 vol.% and was comparable to current literature<sup>28,32</sup>. We attribute this increase to an increasingly crystalline organic blend at higher GOS:Tb fractions. This would also explain the decreasing series resistance of the devices that occurred at high GOS:Tb filling. The mobility values imply charge carrier drift lengths around 74  $\mu\text{m}$ .

Synchrotron grazing incidence wide angle X-ray scattering (GI-WAXS) annealing studies have been performed to study the changes in polymer microstructure induced by GOS:Tb<sup>33,34,35,36</sup>. Fig. 4b shows the diffraction patterns of a 5  $\mu\text{m}$  thick film at a volume ratio of 57 vol.% before and after annealing for 10 min at 150°C and the corresponding out-of-plane line profiles (other filling fractions are shown in Tab. S10). GOS:Tb peak clusters have been indexed according to<sup>37,38,39</sup>. Annealing caused an increase in the domain size of P3HT along the *a* crystal direction (the (100) peak narrows) and a permanent expansion of the *a* lattice constant (the (100) peak position moves to lower *q* values)<sup>35,40</sup>. We also determined a structural interplay between P3HT and GOS:Tb during film drying and annealing. The amount of P3HT face-on lamella increased with GOS:Tb concentration (see Fig. S13). Lamellar parts exhibit improved hole conduction ( $\pi$ -hopping) within the P3HT crystalline domains, and therefore an increase mobility of the X-ray induced charges<sup>35,41</sup>. An explanation may be that the GOS:Tb act as crystallization seed for P3HT, a finding supported by the recent observation of changing morphology upon the incorporation of inorganic particles in a BHJ<sup>42</sup>.

## Conclusion

In this work we have presented, for the first time, a novel approach to fabricate new X-ray imaging devices, involving quasi-direct conversion by incorporation of  $\mu\text{m}$ -scale GOS:Tb scintillator particles directly into an organic semiconductor photoactive layer. X-ray images of the hybrid sensors resolved fine features without optical crosstalk. This was expressed by an excellent spatial resolution of 4.75 lp/mm at MTF=0.2, which is on a par with recent commercial a-Se direct converters. A detailed analysis of the HPD devices reveals an X-ray sensitivity of 459  $\text{e}^-/\text{nGy}_{\text{air}}/\text{mm}^2$  at collection field of -1 V/ $\mu\text{m}$  at volume fractions of the golden filling factor of

67%. At volume fractions above the golden filling factor we observed photoconductive gain at  $1 \text{ V}/\mu\text{m}$ . GI-WAXS and X-CELIV studies clearly correlated the morphology and charge carrier mobility of thick hybrid-devices. Surprisingly, the charge carrier mobility increased with higher volume fractions of GOS:Tb, allowing efficient charge extraction from layer thicknesses of  $10\mu\text{m}$  and above. Spray-coating of thick layers promises to be a low-cost and high throughput production method for large area. This technology can potentially achieve benchmark results compared to today's state-of-the-art direct converters fabricated of a-Se, with the additional benefits of a drastically relaxed demand on external bias, potentially much lower production cost and a higher absorption coefficient for high energy X-ray photons  $>50 \text{ keV}$ .

## Methods

### Device manufacturing:

The device architecture for the reference diodes and imagers is a structured ITO substrate with a TFB (80 nm) interlayer. On top sits an additional pure P3HT interlayer (500 nm), followed by hybrid BHJ containing P3HT:PCBM:GOS:Tb with a weight ratio of 1:1:x ( $x = 0-48$ ), finished by an aluminum top contact. The reference diode area was 1 cm<sup>2</sup> defined by the size of the openings in the passivation layer (SU-8 Photoresist) on top of the ITO contact. After cleaning with N-Methyl-2-pyrrolidone and Mucasol® in an ultrasonic bath the ITO was activated by RIE oxygen plasma for 10min. The TFB interlayer was deposited by spin-coating and annealed for 2 h at 200 °C in a vacuum oven (10<sup>-2</sup> mbar), whereas the P3HT and hybrid BHJ were deposited by spray-coating<sup>2</sup>. The P3HT solution and the hybrid suspension containing P3HT, PCBM and GOS:Tb with a ratio of 1:1:x and total mass content of 2% were stirred for three days (inert atmosphere, at room temperature) and filtered (0.1 μm and 5 μm PTFE, respectively) before spray-coating. The samples were annealed on a hotplate after deposition (nitrogen glove box conditions, 140 °C, 10 min), followed by evacuation process for 24 h in an evaporator (1E-6 mbar). A 0.3 μm thick aluminum top contact was evaporated at an average deposition rate of 0.2 nm/s. After evaporation, an additional annealing step was performed (140 °C; 10 min). Reference X-ray detectors were established by processing a 650 nm layer of P3HT:PCBM on the TFT panels and evaporating a semi-transparent calcium:silver (Ca:Ag) top contact. All devices were protected with a 100μm quartz glass against oxygen and moisture. A commercial-grade 300μm CsI:Tl scintillator screen was then glued with epoxy onto the image detector in order to record X-ray images.

### Image read-out and processing:

Images from the 256x256 TFT panel were read by a read-out IC (ROIC). The signal at the input was simultaneously integrated, amplified, low pass filtered and analog-to-digital converted with a 14 bit converter. The integrator feedback capacitance  $C_f$  was 1 pF, the integration time 20 ms. Noise produced by the external readout electronics TFT detector panel was characterized by taking dark images without and with sensor. To eliminate fixed pattern noise, two different dark images were subtracted. The mean value and the standard deviation were deduced from a *region of interest*

(ROI). The standard deviation presents the electronic noise in numbers of electrons. The noise of the electronic read out circuit was 8.000 electrons. X-ray recordings from objects were off-set compensated by subtracting a dark image and flat-field corrected by calculating the gain factor of each pixel from a flat-field image.

The modulation transfer function MTF is determined by the slanted edge method. First an object with a sharp edge is placed on the X-ray detector and the edge profile is derived from the resulting X-ray image. The Line Spread Function (LSF) is derived by differentiating the edge profile. The Fourier Transform of the LSF defines the MTF.

### Optoelectronic device and material characterization

Absorption data of the BHJ was measured with a Perkin Elmer Spectrometer UV-VIS Lambda 2, IV/IE characteristics were measured by a Keithley 6487 picoamperemeter, X-ray dose rates were measured with a PTW Diados dosimeter, and profile data were measured with a KLA Tencor PT15. X-ray radiation was generated by a rotating anode X-ray tube. The spectrum of the bremsstrahlung corresponds to a tungsten anode and was filtered by 2.5mm aluminum. The stated dose is the entrance-dose-in-air, measured in air at the surface of the sample. An acceleration voltage of 70 kV between glowing cathode and tungsten anode was used to generate the X-ray photons. The air KERMA or entrance-dose-in-air is commonly used in medical applications to give a measurement parameter for the dose a patient is exposed to. This parameter is used to calculate the patient or organ dose. Therefore the entrance-dose-in-air in  $\text{mGy}_{\text{air}}$  allows a comparison with any other medical detector. A detailed description of the dose calculations in medical imaging is presented in the report of the International Commission on Radiation Units (ICRU)<sup>20</sup>. Alternatively, the units of the X-ray sensitivity  $S$  given in  $(\text{e}^-/\text{nGy}_{\text{air}}/\text{mm}^2)$  can be also expressed in  $(\text{e}^-/\text{photons}/\text{keV})$ . This can be done by substitute the  $1 \text{ nGy}_{\text{air}}$  with  $803 \text{ photons} \cdot \text{keV}/\text{mm}^2$  (see Supplementary Information for details).

The emission spectrum of GOS:Tb was measured with a Varian Cary Eclipse spectrometer. A thin powder layer (0.5 mm) was enclosed in a highly reflecting Teflon holder and excited by a narrowband 227 nm UV-source. The emitted light was spectrally filtered and detected by a photomultiplier tube using an emission slit of 2.5 nm.

Further information concerning focus ion beam preparation (FIB) and scanning electron microscopy (SEM), X-ray excited Charge carrier Extraction by Linearly Increasing Voltage (X-CELIV) and Synchrotron grazing incidence wide angle X-ray scattering (GI-WAXS) are described in detail in the Supplementary Information.

### *Acknowledgements*

We would like to thank the German Federal Ministry for Education and Research (BMBF) for funding this work (13N12377).

Patric Büchele is recipient of an Ernst von Siemens Doctoral Fellowship (Ernst-von-Siemens-Promotionsstipendium, EvS).

M. Richter would like to thank the German Research Foundation (DFG) for financial support through the Graduate School GRK 1896.

We would like to thank Dr. Bailey Curzadd (New York University, Abu Dhabi) for contributing with the design of a new GI-WAXS chamber and for fabricating the chamber itself. We thank the XMaS beamline team for the support at the beamline.

Genesis N. Ankah and Tobias Kraus thank Eduard Arzt for his continuing support of the project.

## *Supplementary Information:*

### *1. X-ray images of the HPDs X-ray imaging devices and stacked reference X-ray imaging devices.*

The lifetime of the X-ray imagers was monitored by taking X-ray images throughout 22 months (Fig. S1). No significant degradation was observed due to X-ray radiation. Some minor degradation at the edges due to humidity through the epoxy/glass encapsulation is observable.

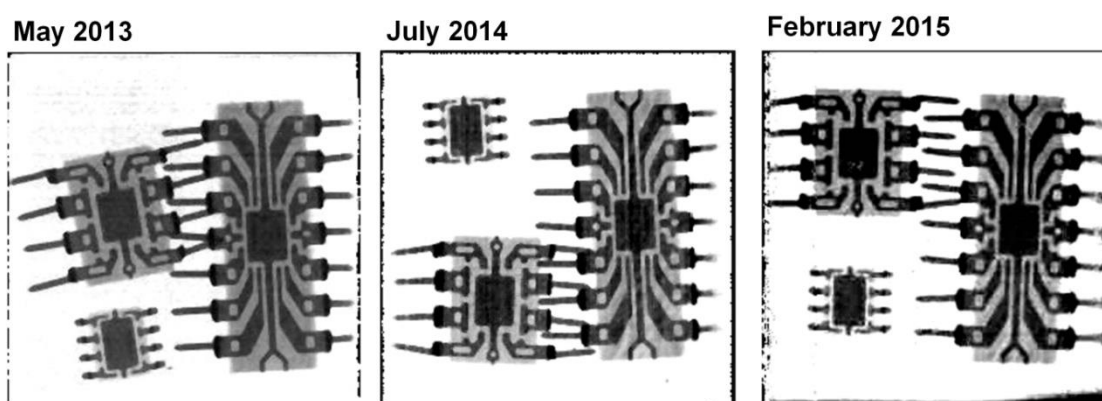


**Figure S1** | Shelf lifetime of one of the X-ray image detector with GOS:Tb volume of 57% (1:1:16) and thickness of 8 $\mu$ m.

The resolution of the HPD devices was compared to reference systems which consisted of a thin-film OPD detector, stacked with a 80 $\mu$ m GOS:Tb film and a 300 $\mu$ m CsI:Tl screen (Fig. S2). The resolution of this reference system is slightly worse than the ideal performance of a CsI:Tl screen due to the encapsulation glass between the scintillator screen and the OPD array which increases the optical crosstalk<sup>4</sup>. However, also commercial detectors suffer from this, as they require a relatively thick epoxy layer between the screen and the array in order to compensate thickness variations in the screen.

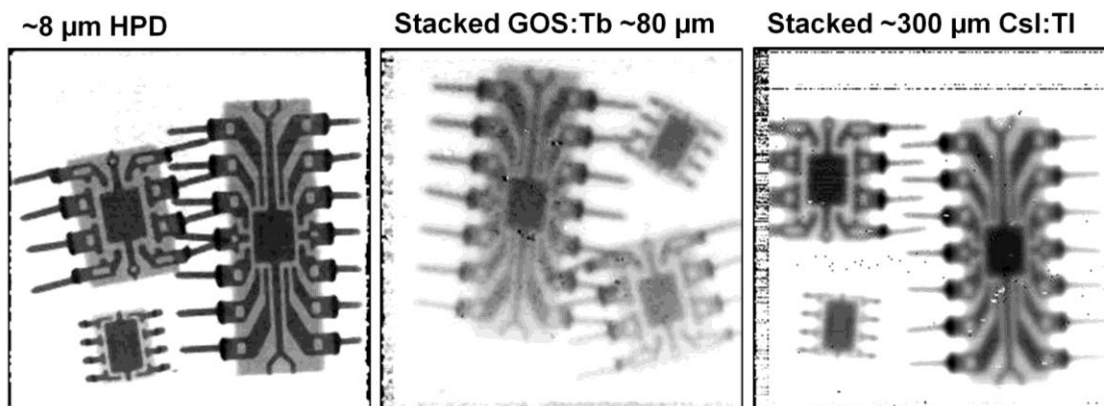


**Figure S2** | Comparison of images taken with different device concepts. A hybrid photodetector with 8  $\mu\text{m}$  photoactive layer thickness and two stacked devices with 80  $\mu\text{m}$  GOS:Tb and 300  $\mu\text{m}$  CsI:Tl.

## 2. X-ray absorption of HPDs and emission of excited GOS:Tb

### X-ray absorption vs. GOS:Tb loading

The ability to fully absorb incoming X-ray radiation is crucial in order to ensure minimal dose exposure to a patient. Fig. S3 describes the attenuation of X-ray radiation as a function of GOS:Tb content in 10 $\mu\text{m}$  thick hybrid-organic layers. The X-ray radiation corresponds to a bremsstrahlung spectrum created with a tungsten anode at an acceleration voltage of 70 kV and a filtration with 2.5 mm Aluminum. The dose attenuation in all HPDs was determined as follows: first, the entrance-dose-in-air  $I_0$  was measured at the HPD surface with a calibrated Diados dosimeter from PTW Freiburg, next, the dose-in-air  $I_G$  was measured behind a dummy sample consisting of the same layer stack as an HPD but without the hybrid layer (substrate, ITO, interlayer, epoxy glue and encapsulation glass), finally, the dose-in-air  $I_S$  behind an HPD sample was measured. The equation  $I_A = \frac{I_G - I_S}{I_0} * 100$  results in dose attenuation  $I_A$  of the hybrid layer with approximately 10  $\mu\text{m}$  thickness in %.

At the right ordinate the effective attenuation coefficient  $\mu$  of the hybrid layer was calculated from  $\mu = -\frac{(\ln(\frac{100-A}{100}))}{d}$ .

The volume and thickness of the GOS:Tb loadings in the hybrid layer was calculated from the weight ratio of the suspension. The attenuation saturates around 65% GOS:Tb filling because the

geometry of the GOS:Tb does not allow denser packing, the small amount of remaining organic material is not able to fill the space between the GOS:Tb particles. For a hybrid layer with a 1:1:24 (66.3 vol.%) ratio and 10  $\mu\text{m}$  thickness the absorption was measured to be at 3.3%. In comparison, a 103  $\mu\text{m}$  thick layer had a measured absorption of 24%. This demonstrates the non-linear X-ray absorption behavior for increasing layer thickness. The fact that the attenuation depicted in Fig. S3 appears to be linear is attributed to the rather thin hybrid layers. The covered absorption range is just not enough to visualize the Lambert-Beer trend.

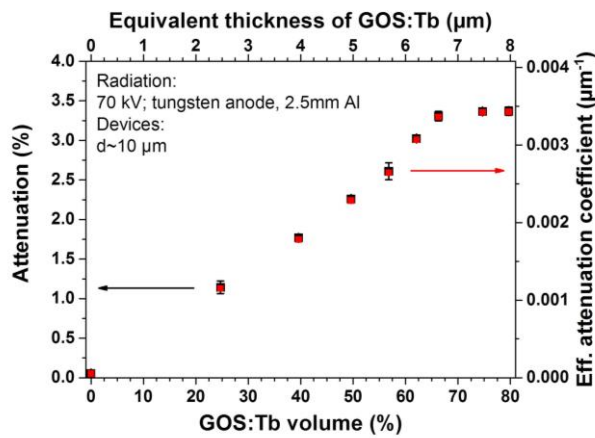


**Figure S3** | Attenuation and the corresponding effective attenuation coefficient of the hybrid photoactive layer of  $\sim 10 \mu\text{m}$  at 70 kV bremsstrahlung filtered with 2.5mm Al. The top axis represents the equivalent thickness of the GOS:Tb in the hybrid layer. The volume and thickness were calculated from the weight ratio of the suspension. Saturation  $>70\%$  occurs because of increased amount of voids between the GOS:Tb particles (densest sphere packing).

### Core shell model (golden filling factor)

The golden filling factor can be calculated by assuming a spherical GOS:Tb particle as the core with an average diameter of  $1.8 \mu\text{m}$  and an organic shell covering the core. The diameter of the GOS:Tb is a fixed value and leads to a volume of  $3.1 \mu\text{m}^3$ . The shell thickness can be varied and the shell material is the BHJ. We suggest that the ideal shell thickness is 130 nm, corresponding to a penetration length of the photons emitted at 532 nm by the GOS:Tb particles in a P3HT:PCBM BHJ of around 130 nm. At this shell thickness, a 532 nm-photon has a minimum probability of  $1 - 1/e^2$  ( $\sim 86\%$ ) to be absorbed before it scatters at the next GOS:Tb particle. Most photons are immediately absorbed and cause a homogeneous charge carrier density distribution throughout the

layer. The calculated volume of the spherical shell with 130 nm thickness is  $1.5 \mu\text{m}^3$  and results in a ratio of 33% organic fraction and 67% inorganic GOS:Tb fractions. The densities of the single components are: P3HT = 1.15 g/ml, PCBM = 1.3 g/ml GOS:Tb = 7.44 g/ml.

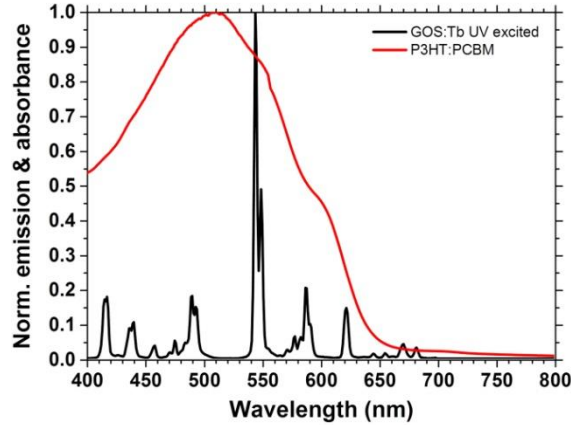


Figure S4 | Normalized emission of UV excited GOS:Tb and normalized absorbance of a P3HT:PCBM layer.

### 3. X-ray-to-electron conversion

In order to compare the measured X-ray sensitivity  $S$  to a model system, we used the simulation of an X-ray spectra and the absorption of GOS:Tb from the NIST XCOM: Photon Cross Sections Database<sup>43,44</sup>. We assumed a device with 10  $\mu\text{m}$ , a filling factor of 50% GOS:Tb, and a bremsstrahlung spectrum of a tungsten anode with 70 kV and 2.5 mm Aluminum filtration (see Fig. S5, left graph).

The attenuation of the 50 vol.% device corresponds to 5  $\mu\text{m}$  pure GOS:Tb. This leads to an absorbed energy per entrance-dose-in-air and device area ( $E_A$ ) in 5 $\mu\text{m}$  solid GOS:Tb of  $E_A = 2.44 \cdot 10^7 \text{ keV/mm}^2/\text{mGy}_{\text{air}}$  (see Fig. S5, right graph).

We considered the measured X-ray sensitivity of  $S = 360 \text{ e}^-/\text{mm}^2/\text{nGy}_{\text{air}}$  of the device with 50 vol.% at -1 V/ $\mu\text{m}$ , which is based on the integrated and offset corrected photo current (see formula 1 and Fig. 3b). The electron-hole-pair generation energy  $W_{\pm}$  can be calculated by dividing the absorbed energy  $E_A$  with the X-ray sensitivity  $S$ :

$$W_{\pm} = \frac{E_A}{S} = \frac{1}{IQE * N/E} = 68eV$$

This value of  $W_{\pm}(HPD\ 50\ vol.\ \%) = 68\ eV$  is well within a reasonable range, as compared with e.g. a-Se which has a  $W_{\pm}(aSe) = 40\ eV$  at an electrical field of  $10V/\mu m$ <sup>6</sup>. An alternative method of calculation the  $W_{\pm}$  is to take the inverse product of the internal quantum efficiency ( $IQE$ ), which expresses the efficiency of extracted electrons per photon in the device, and the average photon response ( $N/E$ ) of GOS:Tb. However, at the moment these parameters are not defined. From literature, we know that the average photo response  $N/E$  of GOS:Tb is  $N/E = 60\ photons/keV$ <sup>45</sup>, but this depends crucially on the particle size<sup>46</sup>. The  $IQE$  can then be used as a fitting parameter in order to match the measured  $S$  by a given  $N/E$ .

Electron-hole-pair generation energy can also be derived from the attenuation in Fig S1. This attenuation can be used to calculate the absorbed energy from the X-ray radiation in the photoactive layer. This leads to the  $W_{\pm}$  plotted in Fig. S6.

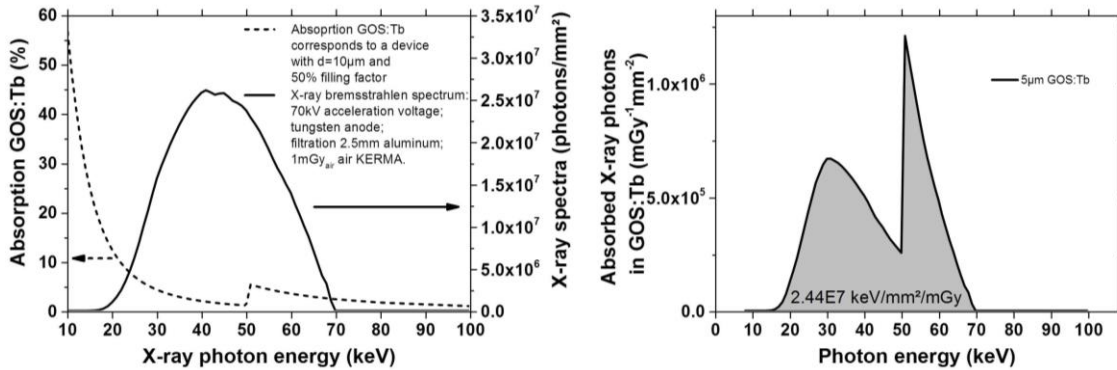


**Figure S5:** Emission spectra of a tungsten anode under an acceleration voltage of 70kV and filtered with 2.5mm Al and in air KERMA of 1mGy (solid line, left graph) and the absorption of a 10μm HPD with an filling factor of 50%, which corresponds to a solid film of 5μm GOS:Tb (dashed line, left graph). The graph on the right side represents the absolute amount of absorbed photons within the 5μm GOS:Tb. The integral of this spectrum equals the total energy deposited per mm<sup>2</sup> and mGy air KERMA.

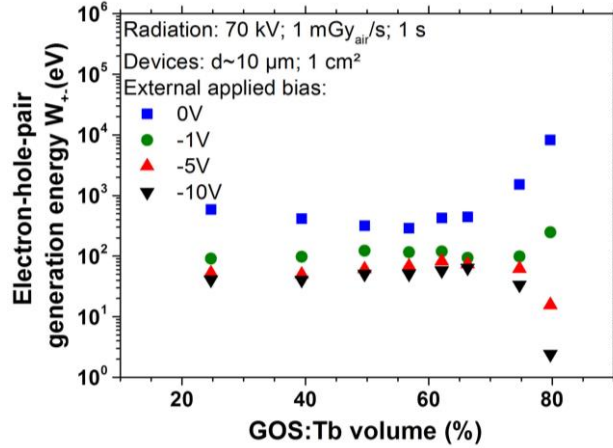


**Figure S6:** Electron-hole-pair generation energy  $W_{\pm} = \frac{E_A}{S}$  derived from the absorbed energy taken from the attenuation in Fig. S1 and the X-ray sensitivity  $S$  from Fig. 3b.

#### 4. Charge transport in thick hybrid devices

X-ray detectors for medical imaging must be able to respond to short X-ray pulses in order to avoid motion blur. Fig. S7 shows the transient current of the hybrid-organic detectors for a pulse length of 1s. For a sample with 57% GOS:Tb filling the rising and falling edge upon switching the X-ray source is clearly visible. The sharp edges are superimposed by a secondary, slower process which we attribute to traps associated to oxygen-doping of the spray-coated films. We hope to improve these transient effects with oxygen-free processing. The difference in the shape between HPDs with different GOS:Tb volume fraction (57% and 80%) may be explained by photoconductive gain<sup>21</sup>. The higher concentration in the suspension give rise to a higher concentration of GOS:Tb at the surface, thus, at the interface to the aluminum top-contact. The contribution to the photoconductive gain can be from GOS:Tb induced traps at the interface and in the bulk. These traps lower the hole injection barrier from the top contact to the P3HT.

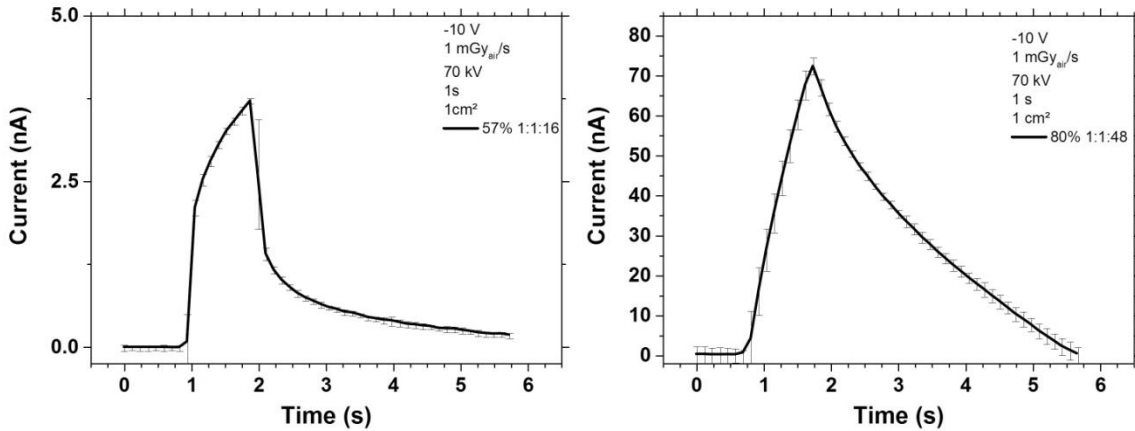


**Figure S7** | X-ray pulse response shape of two HPDs with different GOS:Tb content (1:1:16 and 1:1:48). Dark current is subtracted by end point averaging. The linear increase of the 1:1:48; 80% HPD may be due to photoconductive gain. Error bars result from averaging ten pulses.

The photoconductive behavior of the devices can also be observed in the I-V-characteristics, shown for the 0 vol.% and 80 vol.% device in Fig. S8. A typical indication for a photoconductor is the increased current density in forward bias under exposure (green light and X-rays).

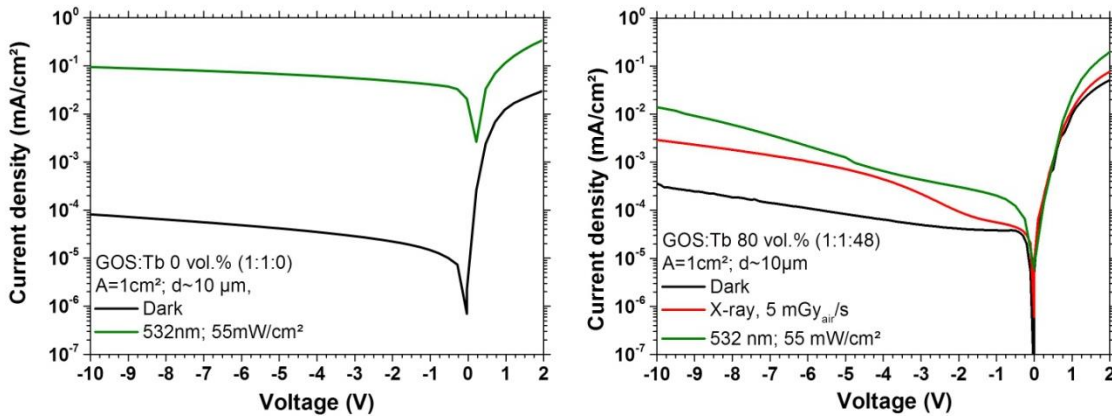


**Figure S8:** Two examples of photoconductive behavior of the 0 vol.% (1:1:0) and 80 vol.% (1:1:48). An influence of light (green and X-ray) in forward bias is shown. The devices behave as a mixture between photodiodes and photoconductors.

### Bias dependence of the X-ray sensitivity

The external bias dependency of the X-ray sensitivity for devices with different filling fraction is plotted in Fig. S9. The X-ray sensitivity at small reverse bias shows high values for the 57 vol.%

device, which is close to the golden filling factor. With increased bias the devices with low loadings of GOS:Tb shows an increased X-ray sensitivity because of bias improved charge carrier extraction. Above the golden filling factor, the X-ray sensitivity increased dramatically when an external field is applied (80 vol.%). This may be explained by a photoconductive gain mechanism as reported before<sup>21</sup>.

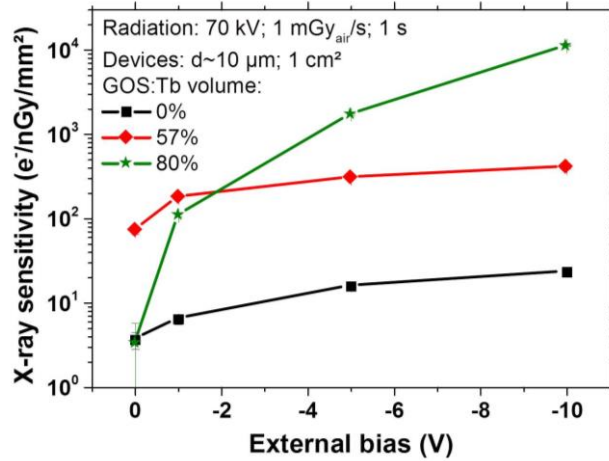


**Figure S9:** X-ray sensitivity for the devices with a volume fraction 0 vol.%, 57 vol.% and 80 vol.% plotted versus the external bias. A higher sensitivity is observed for large reverse bias. The dramatic increase of the 80 % device may be due to photoconductive gain.

### Drift length calculation

For effective charge extraction the drift length  $\delta$  of charge carriers in a semiconducting system must exceed the device thickness. The drift length  $\delta$  is calculated as

$$\delta = \mu \cdot E \cdot \tau \quad (4)$$

where  $\mu$  is the mobility,  $E$  the electrical field and  $\tau$  the charge carrier lifetime. According to Fig. 4a the mobility  $\mu$  of a HPD with 60% GOS:Tb is measured to be  $2 \cdot 10^{-4} \text{ cm}^2/\text{Vs}$ . At the time  $t_{max}$  during extraction, most of the fast charge carriers are extracted. In the inset of Fig. 4a, the peak maximum is at  $t_{max} = 3.7 \text{ ms}$ , which is a measure for the drift time  $\tau_{drift}$  of the charge carriers from their point of origin to the extracting contacts. This drift time is influenced by trapping and de-trapping events that cause values in the ms regime. We therefore took  $\tau_{drift}$  to derive the effective drift

length in the HPD devices. The electrical field strength is approximated by half of the maximum ramp voltage to  $10^4$  V/cm. Thus, the expected effective drift length  $\delta$  is around 74  $\mu\text{m}$ .

### 5. *Experimental details for X-CELIV*

Hybrid photodetectors with a layer thickness of several micro meters require an adaptation of the photo-induced charge extraction by linearly increasing voltage method (photo-CELIV), first applied on organic solar cells by Mozer et al. in 2005<sup>28</sup> and based on the theoretic framework developed by Juška<sup>29</sup>. A voltage ramp was generated by a function generator (Agilent 33500B) and amplified by a 5 MHz high voltage amplifier (Falco Systems WMA-300). The current signal was recorded by an oscilloscope (Tektronix DPO 3034) as a voltage drop over a 10-30 kOhm load resistor, which was additionally amplified by 20 dB (FEMTO HVA 200M 40F). A pulsed X-ray tube was used to excite charges. The mobility  $\mu$  was calculated according to

$$\mu = K^2 \frac{2d^2}{\dot{U}t_{max}^2 \left[ 1 + 0.36 \frac{\Delta j}{j(0)} \right]}, \text{ if } \Delta j \leq j(0), \quad (3)$$

where  $d$  represents for the layer thickness (including the hybrid layer and P3HT interlayer),  $\dot{U}$  is the slope of the voltage ramp in V/s,  $t_{max}$  is the time delay of the current maximum and  $K$  as a pre-factor. According to Juška et al. the factor  $K$  varies between  $1/\sqrt{3}$  for bulk photogeneration and 1 for surface photogeneration of charge carriers<sup>30</sup>. Because only 2.5 % of all X-rays are absorbed by a 10  $\mu\text{m}$  thick HPD (see Fig. S3), which corresponds to an equivalent solid GOS:Tb layer of 5 $\mu\text{m}$ , we used  $1/\sqrt{3}$  to approximate the mobility and account for bulk generation of charge carriers. Because the system is heavily influenced by deep traps, equation (3) is only an approximation. It is well known that traps can have a major impact on the conduction mechanism for organic disordered semiconductors. Assuming an exponential trap distribution within the semiconductor system, Hanfland et al. showed by simulations that the CELIV peak broadens and  $t_{max}$  shifts to longer times for an increasing trap density<sup>47</sup>, and thus derived an uncertainty in the CELIV mobility of 1-2 orders of magnitude, due to traps and a field dependent mobility in typical organic solar cells. We consider our mobility values to be a good estimation, clearly sufficient for a device-to-device comparison and approximation of the charge carrier drift length. We attribute the largest systematic error to the uncertainty in  $d$ , due to the roughness of the top electrode.

The actual recording of the X-CELIV signals for all HPDs (exemplary inset of Fig. 4a) was done for various ramp parameters. The extraction time and peak voltage were varied to reduce the error in determining  $t_{\max}$ . On average, the extraction via voltage ramps took place within 50 ms and at 20 V peak, resulting in a ramp slope  $\dot{U}$  of around 400V/s. Changing the ramp slope did not significantly influence the mobility value as seen by the error bars in Fig. 4a.

## 6. *Grazing-Incidence Wide-Angle X-ray Scattering (GI-WAXS)*

As mentioned above samples with different Gd<sub>2</sub>O<sub>2</sub>S:Tb (GOS:Tb) weight ratios P3HT: PCBM: GOS:Tb (1:1:x, with x ranging from 0 to 36) were deposited on Si/SiO<sub>2</sub> substrates. GI-WAXS measurements were performed at the XMaS beamline (B28, ESRF, Grenoble, France). A nylon/metal-printed chamber equipped with an aluminum hotplate and a spray-coater was mounted onto a 6-circle Huber diffractometer. The sample was mounted onto the compact hotplate via vacuum. Air scattering and background noise were reduced by filling the chamber with helium. Diffraction images were collected with a 2D charge-coupled device detector (MAR SX-165). The X-ray energy was 10 keV. Finally samples were aligned with the reflected beam.

The samples were spray coated and subsequently sealed in inert atmosphere. These samples were unpacked and cut into 4 pieces at the synchrotron and some of them annealed on a hotplate in ambient conditions at 150 °C the same day of the measurements. Measurements on ex-situ as-spun and annealed samples were taken at different incident angles from  $\alpha_i = 0^\circ$  to  $0.5^\circ$ . The Grazing Incidence Wide Angle X-Ray Scattering (GI-WAXS) geometry used in this work is described in reference<sup>33</sup>.

A detailed description of the computer program (GI-XRD-GUI) written for the analysis of the GI-XRD diffraction images is reported in references<sup>33,34,35</sup>. In this work the direction  $q_{xy} = 0$ ,  $q_z = 1 \text{ \AA}^{-1}$  on the diffraction image in Fig. S10 corresponds to the azimuthal angle  $\chi = 0^\circ$  (out-of-plane direction, or OOP), while the direction  $q_{xy} = 1$ ,  $q_z = 0 \text{ \AA}^{-1}$ , corresponds to  $\chi = 90^\circ$  (in-plane direction, or IP). The software was updated with a new routine for total image remapping into the  $q$  space<sup>33</sup>. As a consequence, the cake slice corresponding to  $\chi = 0^\circ$  is not visible in the reported diffraction images (black background). The line profiles shown in Fig. 4b and Fig. S10 were extracted from cake slices at an azimuthal angle  $\chi = 15^\circ$  with an integration aperture of  $\Delta\chi = 10^\circ$ . Peak fitting was performed as reported in<sup>35</sup>. When possible, peak broadening contributions due to

domain size and degree of disorder (g-factor) were separated with the Williamson-Hall fitting procedure<sup>35</sup>. When the Williamson-Hall fitting cannot be performed, estimated domain size is extracted with the Scherrer equation. Limits of this equation are described in<sup>34</sup>. Azimuthal or tangential line profiles (Fig. S11)  $I_{\chi}(\chi)$ , with  $\chi$  ranging from 0 to 90°, were extracted around Debye-Scherrer rings of interest (Fig. S12), as described in<sup>35</sup>.

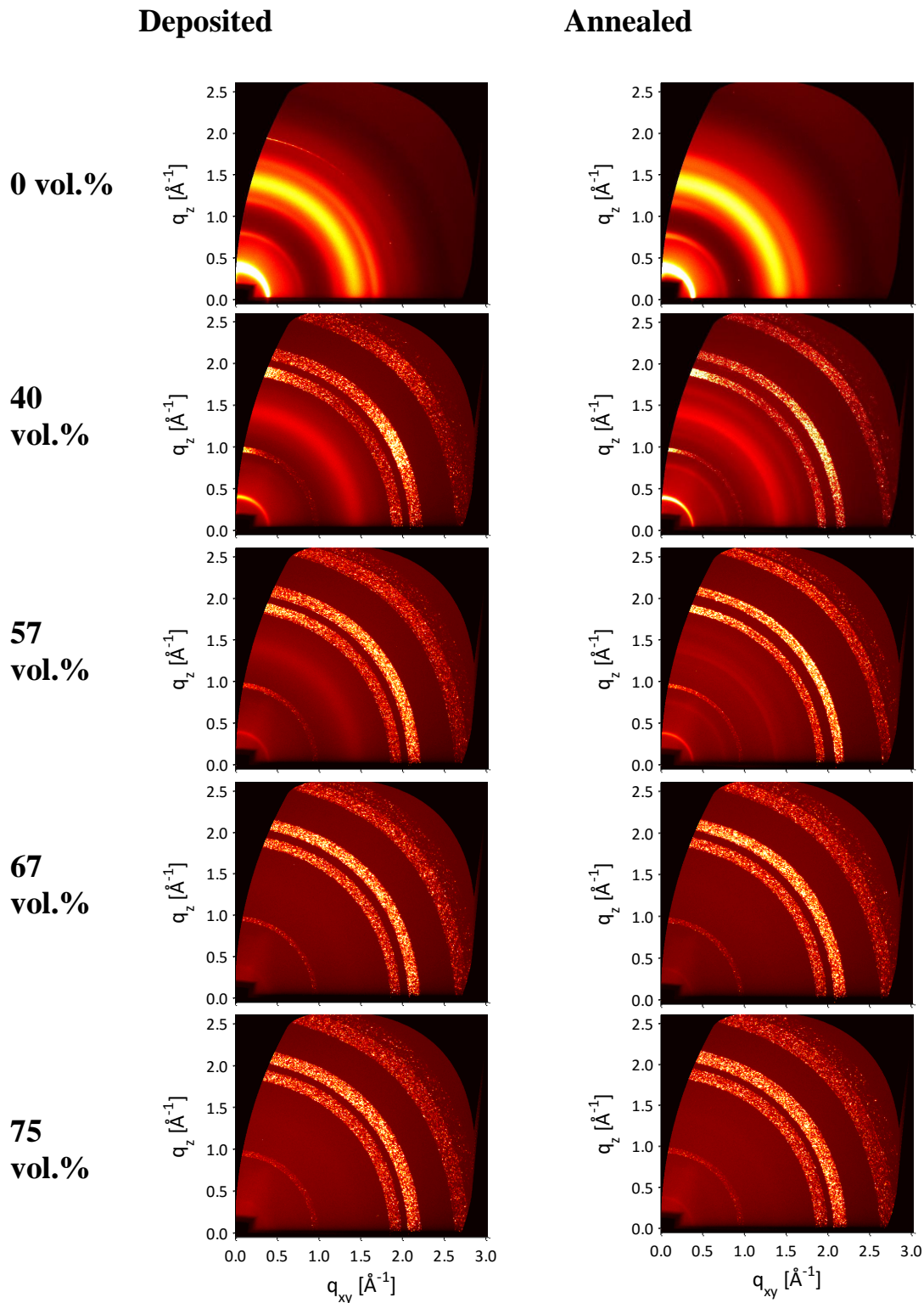


**Table S10:** P3HT:PCBM:GOS:Tb 5  $\mu\text{m}$  thick films deposited on Si/SiO<sub>2</sub> measured ex-situ before and after annealing (10min at 150 °C ), at different P3HT:PCBM:GOS:Tb volume ratios, 1:1:x, where x varies from 0 to 36. Images are collected at  $\alpha_i = 0.24^\circ$ . Figures are resized to 60% from original size.

### OOP Line Profiles $\alpha_i=0.24^\circ$ , $\chi=15^\circ$

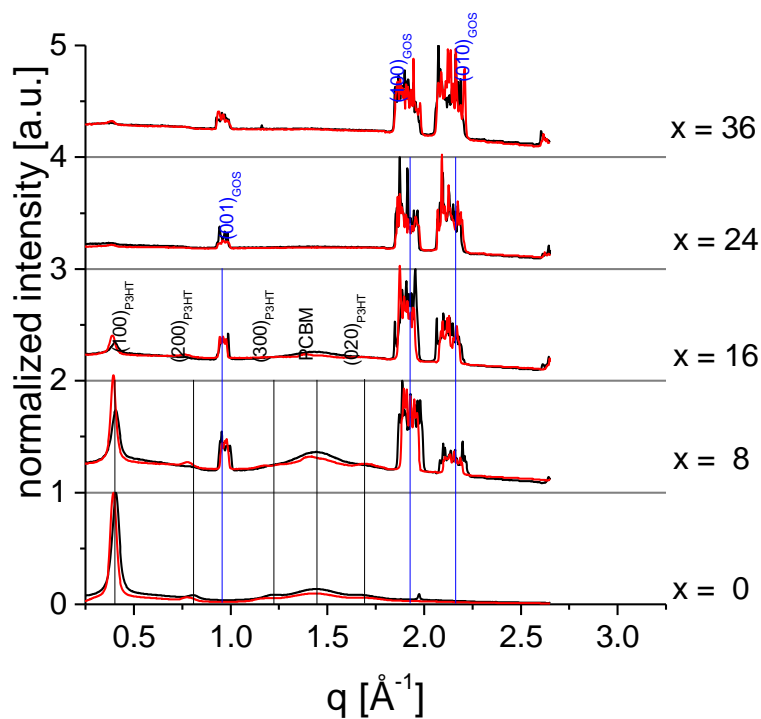


**Figure S11:** Out-of-plane line profiles before (black) and after (red) the annealing for 10 min at 150 °C extracted from diffraction patterns of P3HT:PCBM:GOS:Tb 5  $\mu\text{m}$  films with different weight ratios (1:1: $x$ ,  $0 < x < 36$ ). Intensities have been normalized, while the x-axis represents the absolute value of the scattering vector  $q$ . P3HT:PCBM diffraction patterns resemble patterns reported in our previous works, and peaks have been indexed accordingly<sup>34,35,36</sup>. GOS:Tb crystallizes in the P3 m1 space group, and peaks have been indexed accordingly<sup>37,38,39</sup>.

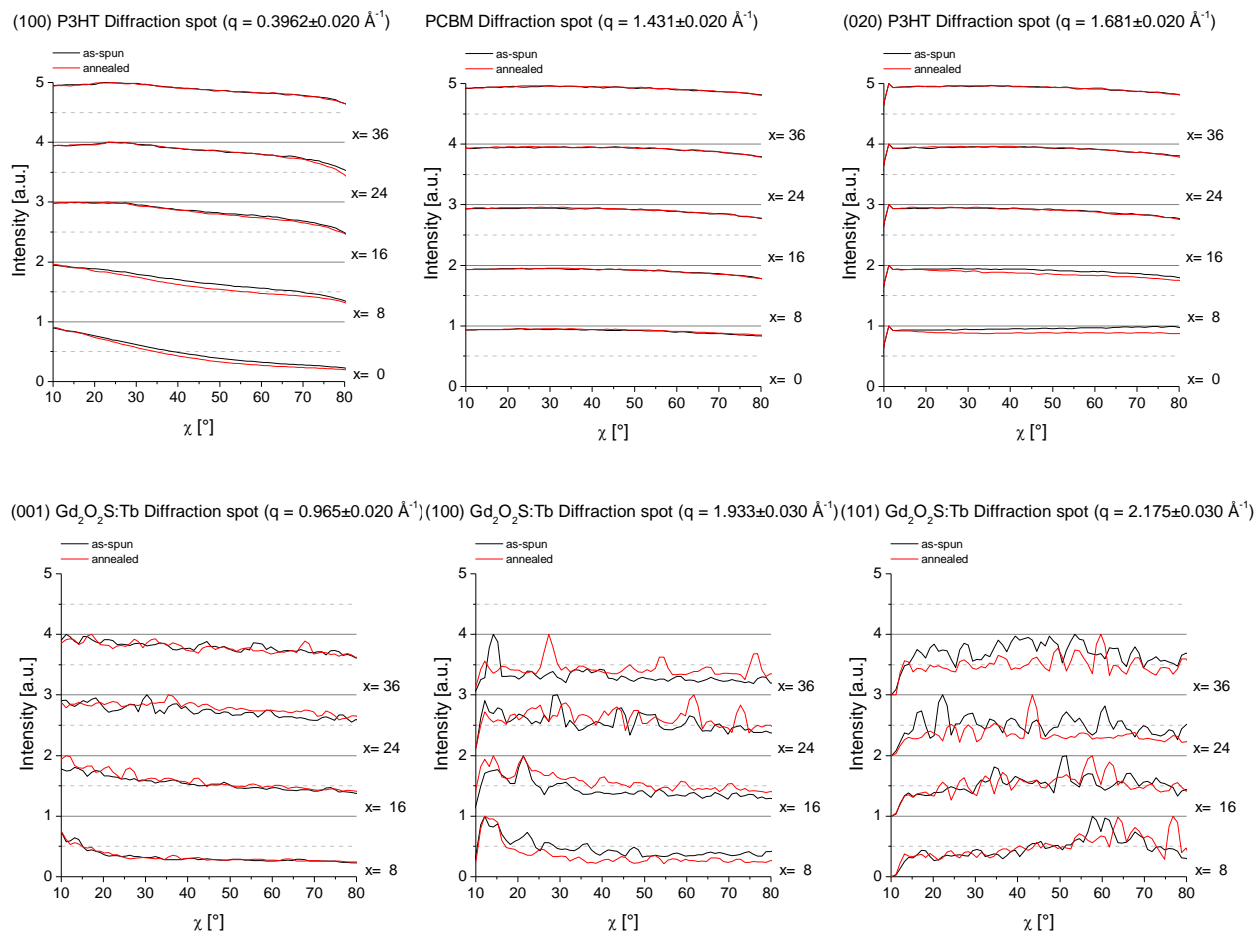


**Figure S12:** Azimuthal line profiles are extracted from the diffraction patterns in Table. S7 along a concentric line from the beam center with the  $q$  range reported above. These line profiles are normalized to their maximum value

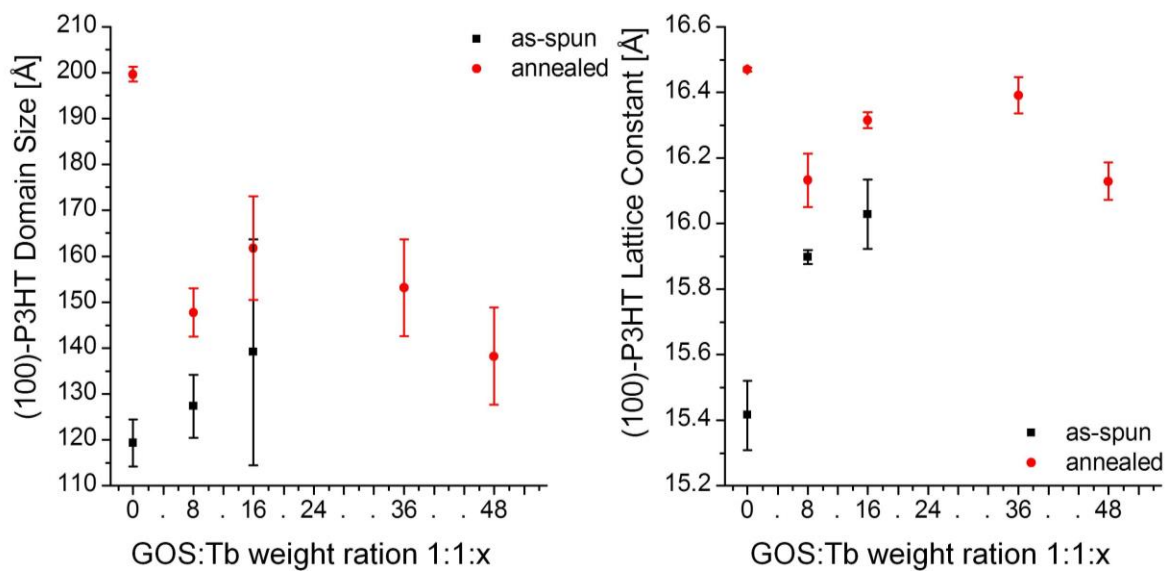


**Figure S13** / Domain size calculated with the Scherrer equation (left) and lattice constant calculated from the OOP-(100)-P3HT peak (line profiles at  $\theta = 15^\circ$ )

## 7. *Additional methods*

### *Structural characterization via focused ion beam preparation and scanning electron microscopy*

Composites of P3HT:PCBM:GOS:Tb were coated with 10 – 20 nm thick Au layers to improve the sample conductivity during electron microscopy. The active layers of the devices consisting of composites of conductive polymers and functional inorganic particles were studied using an FEI Versa 3D DualBeam Focused Ion Beam microscope (FIB). We used FIB to mill into the bulk of a specimen and analyzed its internal microstructure. The FIB was equipped with a Gallium ion source and operated at 30 kV in a current range of 50 pA to 1 nA. FIB cuts through the soft polymer matrix that intersect the hard GOS:Tb particles can cause artifacts in the microstructure such as ridges, grooves, etc. In addition, the high energy ion bombardment may lead to local creation of amorphous layers. Beam damage was minimized and a smooth cross section was achieved using low milling currents of 50-100 pA in a final “cleaning” step. FIB cuts were prepared at several positions of the devices to obtain an overview of the microstructure of the hybrid diode layer. Scanning electron microscopy (SEM) imaging (beam arranged in 52°-tilt angle) was then performed on the cross section to study the distribution of the particles and the occurrences of voids in the composites. The microstructures were analyzed using the secondary electron detector.

## 8. Chemicals:

Poly(3-hexylthiophen-2,5-diyl) (P3HT): Supplier: Rieke Metals, LLC.; molecular weight = 57 k; polydispersity index  $\leq 2.4$ ; regioregularity = 91%

Phenyl-C61-butyric acid methyl ester (PCBM): Supplier: Nano-C Inc.; purity 99.5%

Terbium doped gadolinium oxysulfide (GOS:Tb):  $Gd_2O_2S:Tb$ , Supplier: Nichia Corporation; type: NP-1043; average size: 1.8  $\mu m$ .

Poly[(9,9-dioctylfluorenyl-2,7-diyl)-co-(4,4'-(N-(p-butylphenyl))diphenylamine)] (TFB):  
Supplier: American Dye Source, Inc.; molecular weight: 10000 – 200000.

Chlorobenzene (CB): Supplier: Sigma-Aldrich<sup>®</sup>; ReagentPlus<sup>®</sup>, 99 %

Mucosol<sup>™</sup>: Supplier: Sigma-Aldrich<sup>®</sup>; ReagentPlus<sup>®</sup>, 99 %

1-Methyl-2-pyrrolidinone (NMP): Supplier: Sigma-Aldrich<sup>®</sup>; ReagentPlus<sup>®</sup>, 99 %

## References

- 
- 1 Spahn, M. Flat detectors and their clinical applications. *European Radiology* **15**, 1934-1947, (2005).
  - 2 Pacella, D. Energy-resolved X-ray detectors: the future of diagnostic imaging. *Reports in Medical Imaging* **8**, 1-13, (2015).
  - 3 Kabir, M. Z., *et al.* Direct conversion x-ray sensors: Sensitivity, DQE and MTF. *IEEE Proc.-Circuits, Devices and Systems*, **150**(4), 258-266, (2003).
  - 4 Zhao, W., Ristic, G. & Rowlands, J. A. X-ray imaging performance of structured cesium iodide scintillators. *Medical Physics* **31**, 2594-2605, (2004).
  - 5 Pin, Y., Harmon, C. D., Doty, F. P. & Ohlhausen, J. A. Effect of Humidity on Scintillation Performance in Na and Tl Activated CsI Crystals., *IEEE Transactions on Nuclear Science*. **61**, 1024-1031, (2014).
  - 6 Kasap, S. *et al.* Amorphous and polycrystalline photoconductors for direct conversion flat panel x-ray image sensors. *Sensors*, **11**, 5112-5157, (2011).
  - 7 Kabir, M. Z., *et al.* Effect of repeated x-ray exposure on the resolution of amorphous selenium based x-ray imagers. *Medical physics* **37**(3), 1339-1349, (2010)
  - 8 Kasap, S. O., X-ray sensitivity of photoconductors: application to stabilized a-Se. *J. Phys. D: Appl. Phys.* **33**. 2853-2865, (2000).
  - 9 Gelinck, G. H. *et al.* X-ray imager using solution processed organic transistor arrays and bulk heterojunction photodiodes on thin, flexible plastic substrate. **14**, 2602-2609, (2013).
  - 10 Tedde, S. F. *et al.* Fully Spray Coated Organic Photodiodes. *Nano Letters* **9**, 980-983, (2009).
  - 11 Krebs, F. C. *et al.* A round robin study of flexible large-area roll-to-roll processed polymer solar cell modules. *Solar Energy Materials and Solar Cells* **93**, 1968-1977, (2009).
  - 12 Brabec, C. J. *et al.* Polymer–Fullerene Bulk-Heterojunction Solar Cells. *Advanced Materials* **22**, 3839-3856, (2009).
  - 13 Kraabel, B. *et al.* Ultrafast photoinduced electron transfer in conducting polymer buckminsterfullerene composites. *Chemical Physics Letters* **213**, 389-394, (1993).
  - 14 Heeger, A. J. 25th Anniversary Article: Bulk Heterojunction Solar Cells: Understanding the Mechanism of Operation. *Advanced Materials* **26**, 10-28, (2014).
  - 15 Brabec, C. J., Sariciftci, N. S. & Hummelen, J. C. Plastic Solar Cells. *Advanced Functional Materials* **11**, 15-26, (2001).
  - 16 Rauch, T. *et al.* Near-infrared imaging with quantum-dot-sensitized organic photodiodes. *Nat Photon* **3**, 332-336, (2009).
  - 17 Mills C., A. *et al.* Enhanced x-ray detection sensitivity in semiconducting polymer diodes containing metallic nanoparticles. *Journal of Physics D: Applied Physics* **46**, 275102.
  - 18 Street, R. A. Northrup, J. E., Krusor B. S.. Radiation induced recombination centers in organic solar cells. *Physical review B* **85**, 205211 (2012)
  - 19 Samei, E., Flynn, M. J. & Reimann, D. A. A method for measuring the presampled MTF of digital radiographic systems using an edge test device. *Medical Physics* **25**, 102-113, (1998).

- 20 International Commission on Radiation Units. PATIENT DOSIMETRY FOR X RAYS  
USED IN MEDICAL IMAGING. Journal of the ICRU **5**(2) Report 74. (2005). DOI:  
10.1093/jicru/ndi016
- 21 Chen, H.-Y., LoMichael, K. F., Yang, G., Monbouquette, H. G. & Yang, Y. Nanoparticle-  
assisted high photoconductive gain in composites of polymer and fullerene. *Nat Nano* **3**,  
543-547, (2008).
- 22 Fowler, R. H. & Nordheim, L. *Electron Emission in Intense Electric Fields*. (1928).
- 23 Heeger, A. J., Parker, I. D. & Yang, Y. Carrier injection into semiconducting polymers:  
Fowler-Nordheim field-emission tunneling. *Synthetic Metals* **67**, 23-29, (1994).
- 24 Oehzelt, M., Koch, N. & Heimel, G. Organic semiconductor density of states controls the  
energy level alignment at electrode interfaces. *Nat Commun* **5**, (2014).
- 25 Vázquez, H. *et al.* Barrier formation at metal organic interfaces: dipole formation and the  
charge neutrality level. *Applied Surface Science* **234**, 107-112, (2004).
- 26 Büchele, P., *et al.* Space charge region effects in bidirectional illuminated P3HT: PCBM  
bulk heterojunction photodetectors. *Org. Electron.* **22**, 29-34, (2015).
- 27 Saracco, E., *et al.* Work Function Tuning for High-Performance Solution-Processed Organic  
Photodetectors with Inverted Structure. *Adv. Mater.*, **25**(45), 6534-6538, (2013).
- 28 Mozer, A. J. *et al.* Charge transport and recombination in bulk heterojunction solar cells  
studied by the photoinduced charge extraction in linearly increasing voltage technique.  
*Applied Physics Letters*, **86**(11), 112104. (2005). DOI:10.1063/1.1882753
- 29 Juška, G., *et al.* Extraction Current Transients: New Method of Study of Charge Transport  
in Microcrystalline Silicon. *Phys. Rev. Lett.* **84**, 4946. (2000). DOI:  
10.1103/PhysRevLett.84.4946
- 30 Juška, G., *et al.* Extraction of photogenerated charge carriers by linearly increasing voltage  
in the case of Langevin recombination. *Physical Review B*, **84**(15), 155202. (2011).  
DOI:10.1103/PhysRevB.84.155202
- 31 Nekrašas, N., *et al.* Features of current transients of photogenerated charge carriers, extracted  
by linearly increased voltage. *Chemical Physics*, **404**, pp 56–59. (2012).  
DOI:10.1016/j.chemphys.2012.01.008
- 32 Garcia-Belmonte, g. *et al.* Charge carrier mobility and lifetime of organic bulk  
heterojunctions analyzed by impedance spectroscopy. *Org. Electron.* **9**, pp847-851. (2008)
- 33 Lilliu, S., Alsari, M., Bikondoa, O., Macdonald, J. E. & Dahlem, M. S. Absence of Structural  
Impact of Noble Nanoparticles on P3HT: PCBM Blends for Plasmon Enhanced Bulk-  
Heterojunction Organic Solar Cells Probed by Synchrotron GI-XRD. *Scientific Reports* **5**  
10633 (2015) DOI:10.1038/srep10633.
- 34 Lilliu, S. *et al.* The Influence of Substrate and Top Electrode on the Crystallization Dynamics  
of P3HT:PCBM Blends. *Energy Procedia* **31**, 60-68, (2012).
- 35 Lilliu, S. *et al.* Dynamics of Crystallization and Disorder during Annealing of P3HT/PCBM  
Bulk Heterojunctions. *Macromolecules* **44**, 2725-2734, (2011).
- 36 Lilliu, S. *et al.* Effects of Thermal Annealing Upon the Nanomorphology of Poly (3-  
hexylselenophene)-PCBM Blends. *Macromolecular rapid communications* **32**, 1454-1460,  
(2011).
- 37 Huang, J. *et al.* Gd<sub>2</sub>O<sub>2</sub>S:Eu<sup>3+</sup> and Gd<sub>2</sub>O<sub>2</sub>S:Eu<sup>3+</sup>/Gd<sub>2</sub>O<sub>2</sub>S hollow microspheres:  
Solvothermal preparation and luminescence properties. *Journal of Alloys and Compounds*  
**532**, 34-40, (2012).

- 
- 38 Onoda, M., Chen, X.-a., Sato, A. & Wada, H. Crystal Structure of Cu<sub>2</sub>Gd<sub>2</sub>/3S<sub>2</sub>: Interlayer  
Short-Range Order of Gd Vacancies. *Journal of Solid State Chemistry* **152**, 332-339, (2000).
- 39 Eick, H. A. The Preparation, Lattice Parameters and Some Chemical Properties of the Rare  
Earth Mono-thio Oxides. *Journal of the American Chemical Society* **80**, 43-44, (1958).
- 40 Verploegen, E. *et al.* Effects of Thermal Annealing Upon the Morphology of Polymer–  
Fullerene Blends. *Advanced Functional Materials* **20**, 3519-3529, (2010).
- 41 Pingree, L. S. C., Reid, O. G. & Ginger, D. S. Imaging the Evolution of Nanoscale  
Photocurrent Collection and Transport Networks during Annealing of  
Polythiophene/Fullerene Solar Cells. *Nano Letters* **9**, 2946-2952, (2009).
- 42 González, D. M. *et al.* Improved Power Conversion Efficiency of P3HT: PCBM Organic  
Solar Cells by Strong Spin–Orbit Coupling-Induced Delayed Fluorescence. *Adv. Eng.  
Mater.*, **5**(8), (2015).
- 43 Boone, J., M., Seibert, A., An accurate method for computer-generating tungsten anode X-  
ray spectra from 30 to 140 kV; *Medical Physics* **24**(11), 1661-1670, (1997).
- 44 Berger, M.J., Hubbell, J.H., Seltzer, S.M., Chang, J., Coursey, J.S., Sukumar, R.,  
Zucker, D.S., and Olsen, K., *XCOM: Photon Cross Section Database* (version 1.5).  
<http://physics.nist.gov/xcom> [Monday, 04-May-2015 11:31:38 EDT]. National Institute of  
Standards and Technology, Gaithersburg, MD. (2010).
- 45 Nikl, M., Scintillation detectors for x-rays. *Meas. Sci. Technol.* **17**, R37-R54, (2006).
- 46 Litichevskiy, V., Scintillation panels based on zinc selenide and oxide scintillators. *Funct.  
Materials* **18**(3), (2011).
- 47 Hanfland, R., *et al.* The physical meaning of charge extraction by linearly increasing  
voltage transients from organic solar cells. *Appl. Phys. Lett.* **103**, 063904 (2013); DOI:  
10.1063/1.4818267